Working Report 2016-14

Grimsel Test Site — Long-Term Cement Studies. Reactive Transport Modeling of Experiment 2 at Grimsel.

Maarten W. Saaltink
Josep M. Soler

April 2016

POSIVA OY
Olkiluoto
FI-27160 EURAJOKI, FINLAND
Phone (02) 8372 31 (nat.), (+358-2-) 8372 31 (int.)
Fax (02) 8372 3809 (nat.), (+358-2-) 8372 3809 (int.)

Working Report 2016-14

Grimsel Test Site — Long-Term Cement Studies. Reactive Transport Modeling of Experiment 2 at Grimsel.

Maarten W. Saaltink
Associated Unit: Hydrogeology Group (UPC-CSIC)
Dept. of Civil and Environmental Engineering (UPC)

Josep M. Soler
Associated Unit: Hydrogeology Group (UPC-CSIC)
Institute of Environmental Assessment and Water Research (IDAEA-CSIC)

April 2016

GRIMSEL TEST SITE – LONG-TERM CEMENT STUDIES. REACTIVE TRANSPORT MODELING OF EXPERIMENT 2 AT GRIMSEL.

ABSTRACT

Within the framework of the GTS-LCS project (Grimsel Test Site – Long-Term Cement Studies), an in-situ experiment lasting about 5 years was started in 2009 to study water-cement-rock interactions in fractured granite. A solid cement source (OPC) was installed in a borehole intersecting a water conducting fracture. Two other boreholes at about 0.56 m (observation) and 1.12 m (extraction) from the emplacement borehole were used to monitor the evolution of water composition in the fracture. Prior to the experiment, a tracer test was performed to characterize the initial flow and transport properties of the rock around the experimental boreholes. The flow and reactive transport calculations have been performed using the Retraso-CodeBright code. Solute transport is assumed to be controlled by diffusion in the cement and by advection-dispersion in the rock fracture.

Initially, the flow model calculated from the results of the pre-emplacement tracer test, assuming a homogeneous fracture, was used to model reactive transport after emplacement of the cement. Since the small grid size from the flow model led to excessive computational times, the domain was divided into (a) a 1D radial model for the emplacement borehole and a small volume of rock around it, and (b) a 2D model for the rest of the domain. The results from (a) were used as input for (b).

The model results show dissolution of portlandite and C-S-H in a thin (mm) external layer of the cement (emplacement borehole). In the rock fracture there is dissolution of the primary silicates (except phlogopite) and precipitation of C-S-H, C-A-S-H and calcite. Fracture porosity is reduced in a belt around the 3 boreholes, converging at the extraction borehole (due to the magnitude of the extraction flow rate). The decrease in porosity, due mainly to the precipitation of calcite, is stronger right next to the extraction borehole, due to the more favorable mixing conditions between Grimsel groundwater and cement porewater. The changing water injection rate conditions in the emplacement borehole lead to changes in the flow field and in the position of the mineral reaction fronts.

Keywords: Grimsel, portlandite, granite, fracture, reactive transport modeling.

GRIMSELIN TUTKIMUSALUE – SEMENTIN PITKÄAIKAISTUTKIMUKSET. KOE 2:N REAKTIIVINEN KULKEUTUMISMALLINNUS.

TIIVISTELMÄ

GTS-LCS (Grimsel Test Site – Long-Term Cement Studies) projektissa aloitettiin 2009 noin viisi vuotta kestänyt in situ koe vesi-sementti-kallio vuorovaikutusten tutkimiseksi graniitin kallioraoissa. Kiinteä sementtinäyte (OPC) asennettiin kairareikään joka leikkasi vettä johtavaa rakennetta. Kahta muuta kairareikää 0,56 m (seuranta) ja 1,12 m (uutto) etäisyydellä näytteen asennusreiästä käytettiin pohjaveden koostumuksen monitorointiin rakenteessa. Ennen koetta kallion virtaus- ja kulkeutumisominaisuuksia tutkittiin merkkiainekokeella. Virtaus- ja reaktiivinen kulkeutumismallinnuslaskenta tehtiin käyttäen Retraso-CodeBright koodia. Liuoksen kulkeutumisen on oletettu olevan diffuusion kontrolloimaa sementissä ja advektion ja dispersion kontrolloimaan kallionraossa.

Aluksi käytettiin merkkiainekokeen tuloksista laskettua virtausmallia, olettaen kallioraon olevan homogeeninen, ja mallinnettiin kairareikään asennetun sementti-näytteen reaktiivista kulkeutumista. Koska mallinnusverkon pieni koko johti pitkiin laskenta-aikoihin mallinnusalue jaettiin (a) 1D malliin sementtinäytteen kairareiälle ja pienelle kalliotilavuudelle sen ympärillä (b) 2D malliin lopulle mallinnusaluetta. Tuloksia (a):sta käytettiin (b):n lähtötietoina.

Mallinnustulokset osoittavat portlandiitin ja C-S-H:n liukenemista ohuella alueella sementin ulkoreunaa. Kallioraossa tapahtui primääristen silikaattien (paitsi flogopiitin) liukenemista ja C-S-H:n, C-A-S-H:n ja kalsiitin saostumista. Kallioraon huokoisuus pieneni 3:n kairareiän ympärillä, kohdaten uutto kairareiän kohdalla (johtuen veden virtauksen voimakkuudesta). Huokoisuuden pieneneminen, joka johtui pääosin kalsiitin saostumisesta, oli voimakkaampaa aivan uutto kairareiän läheisyydessä, johtuen Grimselin vesien ja sementistä liukenevien vesien suotuisemmista sekoittumisolo-suhteista. Vaihtelut veden injektointinopeudessa sementtinäytteelle johti muutoksiin virtauskentässä ja mineraalien reaktiorintamissa.

Avainsanat: Grimsel, portlandiitti, graniitti, rako, reaktiivinen kulkeutumismallinnus.

TABLE OF CONTENTS

ABSTRACT

TIIVISTELMÄ

1 INTRODUCTION 2

2 REACTIVE TRANSPORT CODE AND MATHEMATICAL FORMULATION 4

3 CONCEPTUAL MODEL 6
3.1 Modeling approach 6
3.2 Chemical system 6
3.2.1 Cement and rock composition.....6
3.2.3 Thermodynamic data.....8
3.2.4 Reaction rates.....11
3.3 One-dimensional radial model 11
3.4 Two-dimensional model 13

4 RESULTS AND DISCUSSION 16
4.1 Characteristic times 16
4.2 One-dimensional radial model 17
4.3 Two-dimensional model 23

5 CONCLUSIONS 31

ACKNOWLEDGEMENTS.....32

REFERENCES 33

1 INTRODUCTION

Within the framework of the GTS-LCS project (Grimsel Test Site – Long-Term Cement Studies), an in-situ experiment lasting about 5 years was started in 2009 at the Grimsel underground rock laboratory. The objective was the study of water-cement-rock interactions and their effect on water flow and solute transport properties. Pre-hardened Ordinary Portland Cement cylindrical pieces were placed in a borehole intersecting fracture F16. Another two boreholes (namely observation and extraction boreholes) were placed at about 0.56 and 1.12 meters away from the emplacement borehole (Fig. 1). A fourth borehole (07.001) was only poorly hydraulically connected to the other boreholes (not taken into account in the calculations). Grimsel groundwater was circulated and injected in the emplacement borehole. Water was extracted at the observation and extraction boreholes and the chemical composition of the different solutions was monitored. Elevated pH and solute concentrations reflecting interaction with the cement were observed in the observation and extraction boreholes after injection was started in the emplacement borehole.

Prior to the experiment, a tracer test was performed to characterize the initial flow and transport properties of the rock around the 3 experimental boreholes. The interpretation of this test using a two-dimensional homogeneous fracture model was reported by Manette et al. (2015). In this study, reactive transport calculations corresponding to the formation of a high-pH plume and its interaction with the rock have been performed. The model takes into account the total volumes of water at the different boreholes (1.16 L, 1.07 L, 0.32 L at emplacement, observation and extraction, respectively), and the changing injection (emplacement borehole) and extraction (observation and extraction boreholes) flow rates during the experiment. Monitoring data from the 3 different boreholes (pH and major-element chemical composition) have been used to calibrate or otherwise check the performance of the model.

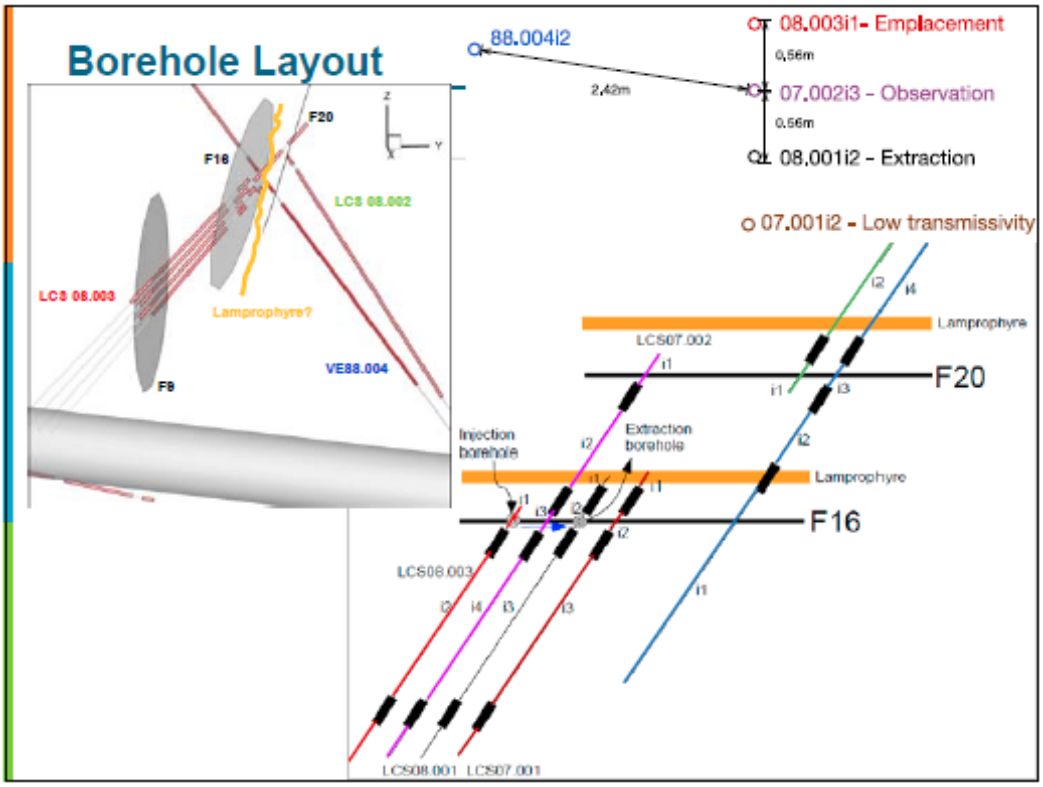

Figure 1. *Experimental setup. Three boreholes (emplacement, observation, extraction) intersect the F16 fracture. After Lanyon and Giroud (2016).*

2 REACTIVE TRANSPORT CODE AND MATHEMATICAL FORMULATION

Reactive transport calculations were performed using the Retraso-CodeBright software package (Olivella et al., 1996; Saaltink et al., 2004), which uses a finite element spatial discretization. Regarding flow, the formulation presented here assumes fully saturated steady state conditions and constant temperature. The flow of water, **q**, is calculated using Darcy's law neglecting the buoyancy term

$$\mathbf{q} = -\frac{\mathbf{k}}{\mu}\nabla P \tag{1}$$

where **k** is the intrinsic permeability tensor (m^2), μ is the dynamic viscosity ($8.9 \cdot 10^{-4}$ Pa s at 25°C) and P is the water pressure (Pa).

Concerning reactive transport, we consider the transport of solutes by means of advection, dispersion and diffusion and both complexation of aqueous species (at equilibrium) and precipitation/dissolution of minerals (kinetics). Then, the mass balance for chemical components has the form

$$\frac{\partial \phi u_{a,i}}{\partial t} = -\nabla \cdot \mathbf{q} u_{a,i} + \nabla \cdot \left(\phi \mathbf{D} \nabla u_{a,i}\right) - R_i \quad i = 1,...,n_c \tag{2}$$

where subscript i refers to the chemical component, u_a (mol m^{-3} water) is the total aqueous concentration of a component, ϕ is the porosity, **D** is a tensor for both diffusion and dispersion (m^2 s^{-1}), R is the precipitation-dissolution rate for a component (mol m^{-3}_porous medium s^{-1}) and n_c is the number of chemical components.

The diffusion-dispersion coefficient is expressed by

$$\mathbf{D} = D_p \mathbf{I} + \mathbf{D}_{dis} \tag{3}$$

where **I** is the identity matrix, D_p is the pore diffusion coefficient (m^2 s^{-1}) and $\mathbf{D}_{dis}$ is the dispersion tensor (m^2 s^{-1}) which can be calculated from the velocities of the water ($\mathbf{v} = \mathbf{q}/\phi$) in 2D from

$$\mathbf{D}_{dis} = \begin{pmatrix} \dfrac{\alpha_L v_x^2 + \alpha_T v_y^2}{|\mathbf{v}|} & \dfrac{(\alpha_L - \alpha_T) v_x v_y}{|\mathbf{v}|} \\ \dfrac{(\alpha_L - \alpha_T) v_x v_y}{|\mathbf{v}|} & \dfrac{\alpha_L v_y^2 + \alpha_T v_x^2}{|\mathbf{v}|} \end{pmatrix} \tag{4}$$

where α_L and α_T are the longitudinal and transversal dispersivities (m).

Total aqueous concentrations of chemical components (u_a) are calculated from the concentrations of primary and secondary aqueous species (c_{a1} and c_{a2}) and stoichiometric coefficients of complexation reactions (S_a)

$$u_{a,i} = c_{a1,i} + \sum_{j}^{n_x} S_{a,ji} c_{a2,j} \quad i = 1,...,n_c \tag{5}$$

where subscript j refers to the aqueous complexes or secondary species, and n_x is the number of aqueous complexation reactions. The concentrations of secondary species are calculated from the primary species through the mass action law

$$\log c_{a2,j} + \log \gamma_{a2,j} = \sum_{j}^{n_x} S_{a,ij} \left(\log c_{a1,j} + \log \gamma_{a1,j} \right) - \log K_{x,j} \quad j = 1,...,n_x \tag{6}$$

where K_x is the equilibrium constant and γ is the activity coefficient which is calculated from the ionic strength (I in mol/kg_H_2O) through the extended Debye-Hückel equation

$$\begin{aligned} \log \gamma_k &= \frac{-Az_k^2 \sqrt{I}}{1 + B\mathring{a}_k \sqrt{I}} + bI \\ I &= \frac{1}{2} \sum_{k}^{n_c+n_x} z_k^2 c_k \end{aligned} \tag{7}$$

where subscript k refers to the aqueous species (both primary and secondary), A, B and b are constants that depend on the temperature and z and $\mathring{a}$ are the charge and ion size of the aqueous species.

Finally, R is calculated from the individual mineral precipitation-dissolution rates (r) using

$$R_i = \sum_{m}^{n_p} S_{p,mi} r_m \quad i = 1,...,n_c \tag{8}$$

The precipitation-dissolution rates, r, are calculated assuming a kinetic approach. For this a kinetic rate law is required, which is a function of all concentrations. In this work we use the rate law of Lasaga (1984), given by

$$r_m = \kappa_m \sigma_m \left(\Omega_m^{\theta} - 1 \right)^{\eta} \sum_{l}^{n_l} a_l^{p_{ml}} \quad m = 1,...,n_p \tag{9}$$

where subscript l refers to a catalyzer, κ is the kinetic rate constant (mol m^{-2} s^{-1}), σ is the reactive surface of a mineral (m^2 of mineral m^{-3} of porous medium), a is the activity of a species, p is the catalyzer coefficient and Ω is the saturation index, which is calculated from

$$\log \Omega_m = \sum_{i}^{n_c} S_{p,im} \left(\log \gamma_{a1,i} + \log c_{a1,i} \right) - \log K_{p,m} \quad m = 1,...,n_p \tag{10}$$

where K_p is the equilibrium constant.

3 CONCEPTUAL MODEL

3.1 Modeling approach

Initially a model was built that used the same setup (geometry, boundary conditions and finite element mesh) as the model to interpret pre-emplacement tracer test 09-03 (Manette et al., 2015). It soon became clear that this setup could not be used for the modeling of reactive transport. A very fine mesh was required near the emplacement borehole, as minerals precipitate in narrow fringes, implying excessive CPU times. Therefore, it was decided to use two models.

A first model simulates the emplacement borehole together with the skin around it. It assumes that during the period without injection the permeability in the skin is low enough to avoid flow of water in it (see Fig. 2). It also assumes that when water is injected, the flow in the skin in only affected by this injection and not by other phenomena (e.g. injection/extraction in other boreholes and natural gradient). In both cases a one-dimensional radial symmetry can be assumed. This reduces significantly the number of nodes and computational times.

A second model simulates the fracture at the scale of all three boreholes (emplacement, observation and extraction) in a two-dimensional domain. It uses as input the results calculated by the 1D radial model (solute concentrations at the outer boundary of the skin of the emplacement borehole).

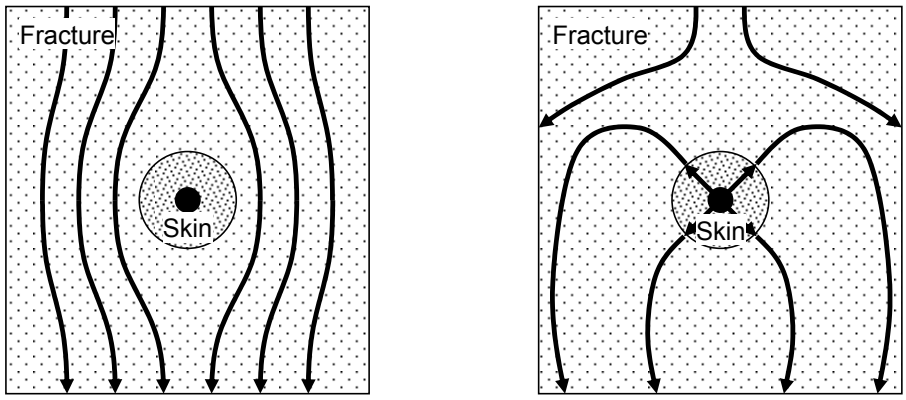

Figure 2. *Illustration of the basic assumptions. During the diffusion period water flows around the skin and there is no water flow within the skin. During injection flow spreads out radially from the borehole.*

3.2 Chemical system

3.2.1 Cement and rock composition

Table 1 shows the initial composition of the cement in the emplacement borehole used in the model. This composition is based on the composition reported by Lothenbach and Winnefeld (2006) for OPC. The volume fractions of the different phases have been modified to account for the porosity of 0.5 estimated from the elevated water/cement ratio of this cement (w/c = 0.8).

Table 2 shows the initial composition of the rock fracture (fault gouge; Soler and Mäder, 2010). It also applies to the zones defined as skins around boreholes.

Table 1. *Initial volume fractions and reactive surface areas for the cement in the emplacement borehole.*

	Vol%	A (m^2/m^3)
Calcite	2.0	10^6
Portlandite	11.7	10^6
CSH-1.67	21.5	10^6
Ettringite	12.6	10^6
Monocarboaluminate	2.3	10^6
Porosity	50	

Table 2. *Initial volume fractions and reactive surface areas for rock fracture (after Soler and Mäder, 2010).*

	Vol%	A (m^2/m^3)
Quartz	19	10730
Albite	14	7920
Microcline	15	8480
Phlogopite	09	5100
Muscovite	22	12420
Porosity	21	

The potential secondary phases that were considered (Soler and Mäder, 2010) were C-S-H solid solution (discretized as phases with Ca/Si 1.4, 1.2, 1.0 and 0.8), brucite, several zeolites (analcime, natrolite, scolecite, stilbite, gismondine, mordenite, wairakite), prehnite (analogue for C-A-S-H), hydrotalcite and several crystalline C-S-H phases (foshagite, gyrolite, hillebrandite, okenite, tobermorite-14A).

3.2.2 Solution composition

Table 3 shows the initial compositions of the cement porewater and the water in the rock fracture (Grimsel groundwater). T = 15°C. The composition of the cement porewater is at equilibrium with the initial solid phases in the cement. Additionally, equilibrium with respect to phlogopite, limiting Mg concentration, has been imposed to

avoid initial supersaturation with respect to this phase. Na and K concentrations were taken from Lothenbach and Winnefeld (2006) but decreased to account for the larger porosity of 0.5 (porosity of the OPC used by Lothenbach and Winnefeld, 2006, was 0.42, as calculated by Savage et al., 2011, using CrunchFlow).

The initial composition of water in the rock fracture (Grimsel groundwater) is based on the composition reported by Soler and Mäder (2010), Mäder et al. (2006) and Eikenberg et al. (1994). Calcite equilibrium has been assumed to calculate the carbonate content. Equilibrium with respect to prehnite (analogue for C-A-S-H) and laumontite have been assumed to limit the concentrations of Al and Si and avoid initial supersaturation with respect to these phases.

Table 3. *Initial compositions (total molalities and pH) for the cement porewater and the water in the rock fracture. T = 15°C.*

	Cement porewater		Rock fracture	
	C_{tot} (molal)	Constraint	C_{tot} (molal)	Constraint
Al	$3.67 \cdot 10^{-5}$	monocarb.	$6.48 \cdot 10^{-7}$	prehnite
CO_3	$2.17 \cdot 10^{-4}$	calcite	$1.78 \cdot 10^{-4}$	calcite
Ca	$8.64 \cdot 10^{-4}$	portlandite	$1.40 \cdot 10^{-4}$	
Cl	$1.00 \cdot 10^{-6}$		$4.60 \cdot 10^{-4}$*	
K	$5.26 \cdot 10^{-1}$		$3.84 \cdot 10^{-6}$	
Mg	$1.78 \cdot 10^{-10}$	phlogopite	$4.11 \cdot 10^{-7}$	
Na	$5.05 \cdot 10^{-2}$		$5.74 \cdot 10^{-4}$	charge
SO_4	$2.93 \cdot 10^{-3}$	ettringite	$5.73 \cdot 10^{-5}$	
SiO_2(aq)	$1.42 \cdot 10^{-4}$	CSH-1.7	$7.60 \cdot 10^{-5}$	laumontite
pH	13.84	charge	9.84	

*The measured value for Cl in the Grimsel groundwater was $1.5 \cdot 10^{-4}$ molal. The different value in the model is due to charge balance issues. The effects are discussed in the results section.

3.2.3 Thermodynamic data

All the chemical equilibria in solution at 15°C (Table 4) were taken from the LLNL database included in the code, which is based on the EQ3/6 database (Wolery et al., 1990). The equilibrium constants for all the mineral reactions are given in Table 5. All the solid equilibrium constants at 15°C were taken from the LLNL database, except for portlandite (Hummel et al., 2002), monocarbonate, ettringite and hydrotalcite (cemdata07 database: Matschei et al., 2007; Lothenbach et al., 2008), and C-S-H (Kulik and Kersten, 2001). The C-S-H solid solution has been introduced in the model as several discrete compositions (different mol fractions of the end-members), with solubilities calculated from the original solid solution model.

Table 4. *Equilibrium constants (log K at 15°C) and stoichiometric coefficients of equilibria in solution. Reactions are written as the destruction of 1 mole of the species in the first column.*

Reaction	log K	Primary species									
		al(oh)4-	ca+2	cl-	co3-2	hsio3-	k+	mg+2	na+	oh-	so4-2
al(oh)2+	16.0512	1.000	0.000	0.000	0.000	0.000	0.000	0.000	0.000	-2.000	0.000
al(oh)3(aq)	8.3143	1.000	0.000	0.000	0.000	0.000	0.000	0.000	0.000	-1.000	0.000
al(so4)2-	29.2892	1.000	0.000	0.000	0.000	0.000	0.000	0.000	0.000	-4.000	2.000
al+3	34.1086	1.000	0.000	0.000	0.000	0.000	0.000	0.000	0.000	-4.000	0.000
aloh+2	25.0999	1.000	0.000	0.000	0.000	0.000	0.000	0.000	0.000	-3.000	0.000
also4+	31.1653	1.000	0.000	0.000	0.000	0.000	0.000	0.000	0.000	-4.000	1.000
ca(h3sio4)2(aq)	-5.1323	0.000	1.000	0.000	0.000	2.000	0.000	0.000	0.000	0.000	0.000
cacl+	0.7044	0.000	1.000	1.000	0.000	0.000	0.000	0.000	0.000	0.000	0.000
cacl2(aq)	0.6032	0.000	1.000	2.000	0.000	0.000	0.000	0.000	0.000	0.000	0.000
caco3(aq)	-3.2271	0.000	1.000	0.000	1.000	0.000	0.000	0.000	0.000	0.000	0.000
cah2sio4(aq)	-5.8692	0.000	1.000	0.000	0.000	1.000	0.000	0.000	0.000	1.000	0.000
cah3sio4+	-1.3012	0.000	1.000	0.000	0.000	1.000	0.000	0.000	0.000	0.000	0.000
cahco3+	2.8700	0.000	1.000	0.000	1.000	0.000	0.000	0.000	0.000	-1.000	0.000
caoh+	-1.0959	0.000	1.000	0.000	0.000	0.000	0.000	0.000	0.000	1.000	0.000
caso4(aq)	-2.0746	0.000	1.000	0.000	0.000	0.000	0.000	0.000	0.000	0.000	1.000
co2(aq)	11.8405	0.000	0.000	0.000	1.000	0.000	0.000	0.000	0.000	-2.000	0.000
h+	14.3380	0.000	0.000	0.000	0.000	0.000	0.000	0.000	0.000	-1.000	0.000
h2sio4-2	-1.1417	0.000	0.000	0.000	0.000	1.000	0.000	0.000	0.000	1.000	0.000
hco3-	3.9148	0.000	0.000	0.000	1.000	0.000	0.000	0.000	0.000	-1.000	0.000
hso4-	12.4785	0.000	0.000	0.000	0.000	0.000	0.000	0.000	0.000	-1.000	1.000
kcl(aq)	1.5848	0.000	0.000	1.000	0.000	0.000	1.000	0.000	0.000	0.000	0.000
khso4(aq)	13.6985	0.000	0.000	0.000	0.000	0.000	1.000	0.000	0.000	-1.000	1.000
koh(aq)	0.1220	0.000	0.000	0.000	0.000	0.000	1.000	0.000	0.000	1.000	0.000
kso4-	-0.8653	0.000	0.000	0.000	0.000	0.000	1.000	0.000	0.000	0.000	1.000
mg(h3sio4)2(aq)	-6.4623	0.000	0.000	0.000	0.000	2.000	0.000	1.000	0.000	0.000	0.000
mg4(oh)4+4	-15.4903	0.000	0.000	0.000	0.000	0.000	0.000	4.000	0.000	4.000	0.000
mgcl+	0.1237	0.000	0.000	1.000	0.000	0.000	0.000	1.000	0.000	0.000	0.000
mgco3(aq)	-2.9210	0.000	0.000	0.000	1.000	0.000	0.000	1.000	0.000	0.000	0.000
mgh2sio4(aq)	-6.9492	0.000	0.000	0.000	0.000	1.000	0.000	1.000	0.000	1.000	0.000
mgh3sio4+	-1.5512	0.000	0.000	0.000	0.000	1.000	0.000	1.000	0.000	0.000	0.000
mghco3+	2.8831	0.000	0.000	0.000	1.000	0.000	0.000	1.000	0.000	-1.000	0.000
mgoh+	-2.2100	0.000	0.000	0.000	0.000	0.000	0.000	1.000	0.000	1.000	0.000
mgso4(aq)	-2.2681	0.000	0.000	0.000	0.000	0.000	0.000	1.000	0.000	0.000	1.000
nacl(aq)	0.8083	0.000	0.000	1.000	0.000	0.000	0.000	0.000	1.000	0.000	0.000
naco3-	-0.6302	0.000	0.000	0.000	1.000	0.000	0.000	0.000	1.000	0.000	0.000
nahco3(aq)	3.6620	0.000	0.000	0.000	1.000	0.000	0.000	0.000	1.000	-1.000	0.000
nahsio3(aq)	-1.7357	0.000	0.000	0.000	0.000	1.000	0.000	0.000	1.000	0.000	0.000
naoh(aq)	0.1516	0.000	0.000	0.000	0.000	0.000	0.000	0.000	1.000	1.000	0.000
naso4-	-0.7869	0.000	0.000	0.000	0.000	0.000	0.000	0.000	1.000	0.000	1.000
sio2(aq)	4.2453	0.000	0.000	0.000	0.000	1.000	0.000	0.000	0.000	-1.000	0.000

Table 5. *Equilibrium constants (log K at 15°C) and stoichiometric coefficients for mineral reactions. Reactions are written as the dissolution of 1 mole of mineral.*

Reaction	log K	Primary species									
		al(oh)4-	ca+2	cl-	co3-2	hsio3-	k+	mg+2	na+	oh-	so4-2
albite	-8.4207	1.000	0.000	0.000	0.000	3.000	0.000	0.000	1.000	-3.000	0.000
k-feldspar	-11.6313	1.000	0.000	0.000	0.000	3.000	1.000	0.000	0.000	-3.000	0.000
phlogopite	-58.2010	1.000	0.000	0.000	0.000	3.000	1.000	3.000	0.000	3.000	0.000
muscovite	-16.1003	3.000	0.000	0.000	0.000	3.000	1.000	0.000	0.000	-5.000	0.000
quartz	0.0231	0.000	0.000	0.000	0.000	1.000	0.000	0.000	0.000	-1.000	0.000
calcite	-8.4182	0.000	1.000	0.000	1.000	0.000	0.000	0.000	0.000	0.000	0.000
portlandite	-5.0755	0.000	1.000	0.000	0.000	0.000	0.000	0.000	0.000	2.000	0.000
brucite	-11.7000	0.000	0.000	0.000	0.000	0.000	0.000	1.000	0.000	2.000	0.000
csh-08	-17.1207	0.000	1.820	0.000	0.000	2.270	0.000	0.000	0.000	1.370	0.000
csh-10	-9.3507	0.000	1.000	0.000	0.000	1.000	0.000	0.000	0.000	1.000	0.000
csh-12	-10.7076	0.000	1.200	0.000	0.000	1.000	0.000	0.000	0.000	1.400	0.000
csh-14	-11.9594	0.000	1.400	0.000	0.000	1.000	0.000	0.000	0.000	1.800	0.000
csh-1667	-13.4795	0.000	1.670	0.000	0.000	1.000	0.000	0.000	0.000	2.340	0.000
analcime	-7.9852	0.960	0.000	0.000	0.000	2.040	0.000	0.000	0.960	-2.040	0.000
laumontite	-16.6560	2.000	1.000	0.000	0.000	4.000	0.000	0.000	0.000	-4.000	0.000
mesolite	-20.6696	1.990	0.657	0.000	0.000	3.010	0.000	0.000	0.676	-3.010	0.000
natrolite	-16.0081	2.000	0.000	0.000	0.000	3.000	0.000	0.000	2.000	-3.000	0.000
scolecite	-18.5429	2.000	1.000	0.000	0.000	3.000	0.000	0.000	0.000	-3.000	0.000
stilbite	-22.3222	2.180	1.019	0.000	0.000	6.820	0.006	0.000	0.136	-6.820	0.000
gismondine	-37.6948	4.000	2.000	0.000	0.000	4.000	0.000	0.000	0.000	-4.000	0.000
mordenite	-6.6626	0.940	0.289	0.000	0.000	5.060	0.000	0.000	0.361	-5.060	0.000
wairakite	-11.9252	2.000	1.000	0.000	0.000	4.000	0.000	0.000	0.000	-4.000	0.000
prehnite	-29.5188	2.000	2.000	0.000	0.000	3.000	0.000	0.000	0.000	-1.000	0.000
foshagite	-33.9203	0.000	4.000	0.000	0.000	3.000	0.000	0.000	0.000	5.000	0.000
gyrolite	-21.2633	0.000	2.000	0.000	0.000	3.000	0.000	0.000	0.000	1.000	0.000
hillebrandite	-15.0717	0.000	2.000	0.000	0.000	1.000	0.000	0.000	0.000	3.000	0.000
okenite	-9.7110	0.000	1.000	0.000	0.000	2.000	0.000	0.000	0.000	0.000	0.000
tobermorite-14a	-52.7703	0.000	5.000	0.000	0.000	6.000	0.000	0.000	0.000	4.000	0.000
hydrotalcite-OH	-56.6656	2.000	0.000	0.000	0.000	0.000	0.000	4.000	0.000	6.000	0.000
ettring-Al10	-46.1057	2.000	6.000	0.000	0.000	0.000	0.000	0.000	0.000	4.000	3.000
monocarb-Al10	-31.8580	2.000	4.000	0.000	1.000	0.000	0.000	0.000	0.000	4.000	0.000

3.2.4 Reaction rates

The rate laws used for the primary minerals in the rock (quartz, albite, microcline, phlogopite, muscovite) are based on those used by Soler and Mäder (2010) for the modeling of the core infiltration experiment in the HPF project (Table 6). Values of θ and η for albite and microcline are from Soler and Lasaga (1998). For all the other phases (cement and secondary phases), large values of the rate constants (10^{-9} mol m^{-2} s^{-1}) and of the surface areas have been used, leading to local equilibrium with respect to those phases.

Table 6. *Rate parameters for the primary minerals in the rock (see eq. 9).*

MINERAL m	$\log \kappa_m$ (mol/m^2/s)	p $\left(a^{p}_{H^+}\right)$	θ	η
Quartz	-13.92	-0.2	1.0	1.0
Albite	-12.92	-0.2	0.4	14
Microcline	-20.22	-0.73	0.4	14
Phlogopite	-13.52	-0.2	1.0	1.0
Muscovite	-13.12	-0.1	1.0	1.0

The initial composition of the Grimsel groundwater in the model was initially supersaturated with respect to mesolite, scolecite, stilbite and gismondine. Therefore, large supersaturation thresholds were imposed for those phases (Ω = 3900, 230, $1.8 \cdot 10^5$, 190, for mesolite, scolecite, stilbite and gismondine, respectively), preventing their precipitation.

3.3 One-dimensional radial model

The geometry of the 1D radial model is shown in Figure 3. The domain is discretized in 101 1D finite elements with sizes ranging from 0.1 mm near the gap between cement and rock to 1.5 mm near the skin-fracture interface. Like in the model of Manette et al. (2015), the total volume of water in the circulation system (tank, tubing, gap) is taken into account by rescaling the porosity. The same is done for the cement which has a thickness larger than the fracture. This assumes that concentrations are the same in the direction of the borehole perpendicular to the fracture (well-mixed conditions).

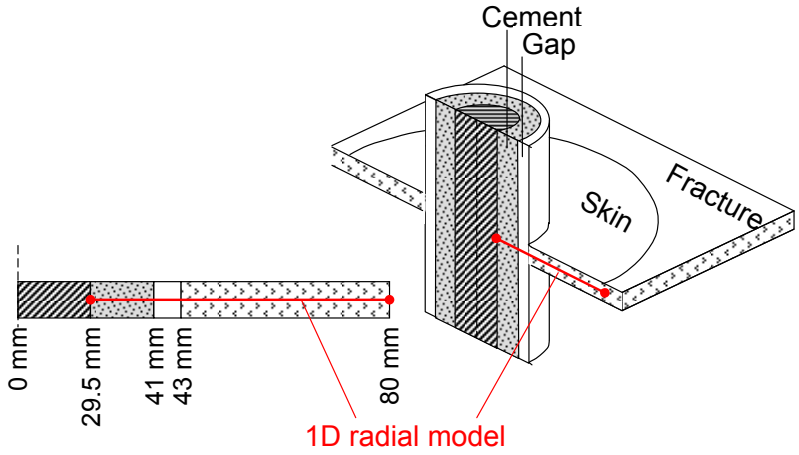

Figure 3. *Scheme of the 1D radial model.*

Table 7 displays the transport parameters of the model with both the real and rescaled porosities. The gap is assumed to only contain water. Porosity for the fracture is taken from Soler et al. (2006) and Soler and Mäder (2007), corresponding to the porosity of the fault gouge in a granite core from Grimsel. Cement porosity was estimated to be 0.5, which is in agreement with reported porosities for cements with the same water/cement ratio of 0.8 (Walker, 2016). The diffusion coefficient for the skin (rock fracture) is based on common values in the literature. The diffusion coefficient of the cement was also based on previous values in the literature. For instance, Trapote-Barreira et al. (2016) found values of D_p from $2 \cdot 10^{-13}$ to $9 \cdot 10^{-13}$ m^2 s^{-1} for diffusion of cement components in mortar grains (mortar porosity ϕ = 0.125) in column experiments. However, reported values from through-diffusion experiments in cement paste using HTO and Cl^- are much higher (D_p values about $6 \cdot 10^{-10}$ and $2 \cdot 10^{-10}$ m^2 s^{-1} for HTO and Cl^-, respectively, for ϕ = 0.5; capacity factors are about 1.5 and 1.7, respectively; Walker, 2016). Diffusion coefficient and dispersivity of the gap are sufficiently high to ensure perfect mixing within the gap. The dispersivity of the skin (0.02 m) is from Manette et al (2015). The dispersivity assigned to the cement has no effect because there is no flow of water through the cement.

Table 7. *Transport parameters for the 1D radial model. ϕ is porosity, D_p is the pore diffusion coefficient and α is the dispersivity.*

	ϕ_{real}	$\phi_{rescaled}$	D_p (m^2 s^{-1})	α (m)
Cement	0.5	345.0	$2.0 \cdot 10^{-12}$	0.002
Gap	1.0	2205.0	$1.0 \cdot 10^{-5}$	10.0
Skin	0.21	0.21	$1.0 \cdot 10^{-9}$	0.02

In order to simulate the various flow regimes we used the following boundary condition. During the initial diffusion period (August 2009 to October 2010) there is no injection. However, there is flow of water around the skin-fracture interface. This is simulated as an inflow of water into the second node from the end of the domain and an outflow at the last node. This inflow-outflow is calculated from the flow rate at the extraction borehole using

$$q_{skin} 2\pi d_{empl-extr} b = Q_{ext} \tag{11}$$

and

$$Q_{skin} = q_{skin} 2\pi r_{skin} b = Q_{ext} \frac{r_{skin}}{d_{emp-ext}} \tag{12}$$

where q_{skin} (m^3 m^{-2} s^{-1}) is the Darcy velocity at the skin-fracture interface, $d_{emp-ext}$ (m) is the distance between the emplacement and extraction boreholes, b is the thickness of the fracture (10^{-3} m), Q_{ext} (m^3 s^{-1}) is the extraction flow rate at extraction, r_{skin} is the radius of the skin (0.08 m) and Q_{skin} is the flow rate at the skin-fracture interface (m^3 s^{-1}). A value of $2.4 \cdot 10^{-6}$ L s^{-1} is obtained. After this, water is injected at the gap, first with a flow rate of $3.98 \cdot 10^{-6}$ L s^{-1} (between October 2010 and June 2011) and later with a flow rate of $9.83 \cdot 10^{-7}$ L s^{-1} (between June 2011 and September 2014). During the injection period there is no flow of water around the skin-fracture interface. The water injected at the gap simply leaves the system at this boundary.

3.4 Two-dimensional model

The 2D model assumes that the flow of water is only affected by the flow rates at the three boreholes (emplacement, observation and extraction). The initial diffusion period is not included in the 2D model. Only the period when water is injected into the emplacement borehole is taken into account. Like in the conservative tracer test interpreted by Manette et al. (2015) the natural gradients can be neglected due to the high flow rates at these boreholes. This means that the system is symmetrical with respect to the line crossing the center of the three boreholes and only half of the domain has to be modeled. Figure 4 shows the geometry and the finite element mesh which consists of triangular elements with a size of about 2 cm. Also this model explicitly includes the volumes of water in the gaps of the boreholes by rescaling the porosities.

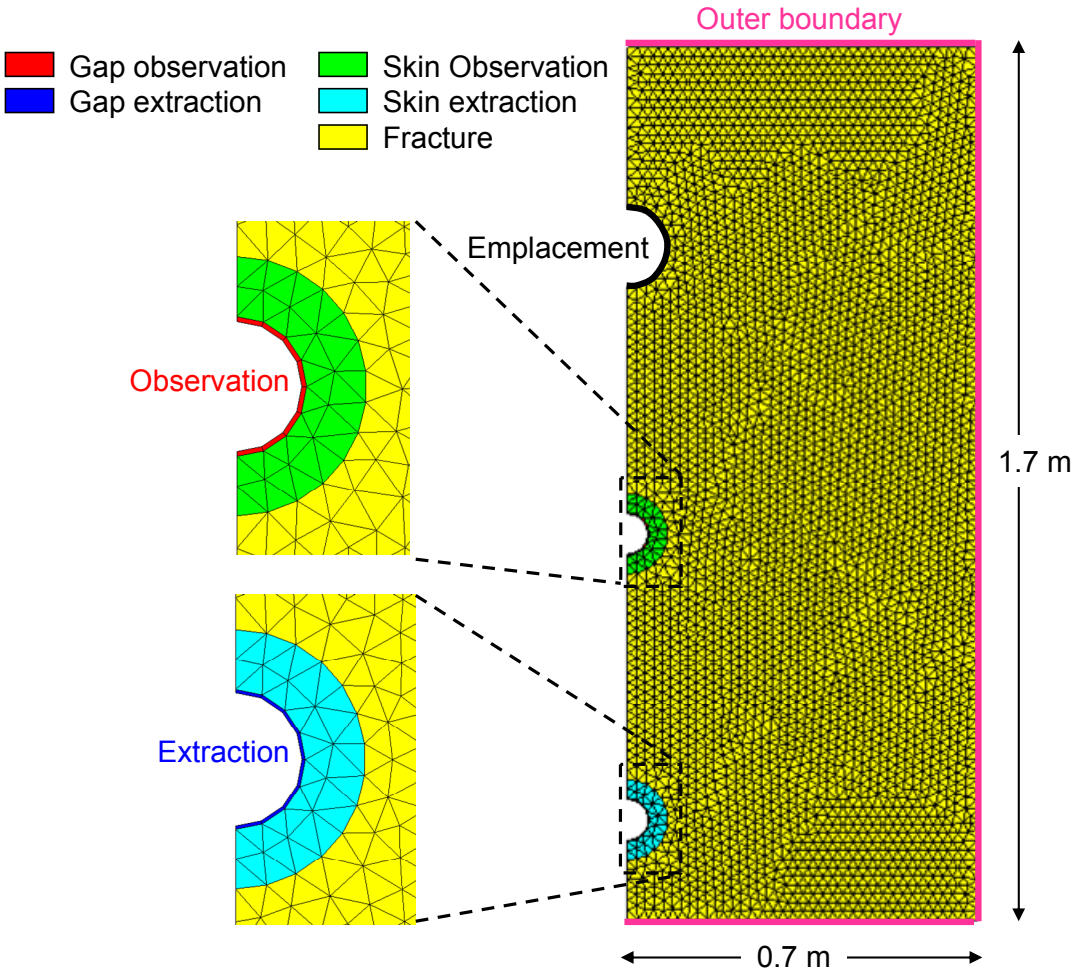

Figure 4. *Geometry and finite element mesh of the 2D model.*

Table 8 shows the flow and transport parameters. Intrinsic permeabilities are taken from Manette et al. (2015). The gaps are assumed to only contain water. Porosities for the skin and fracture are taken from Soler et al. (2006) and Soler and Mäder (2007). Diffusion coefficients of the fracture and skins are the same as in the 1D model, although they do not greatly affect the results as dispersion dominates over diffusion. The dispersivities of the gaps of both boreholes are sufficiently high to ensure perfect mixing. The dispersivites of the skins and fracture have been calibrated to adjust the modeled to the measured pH values.

Table 8. *Transport parameters for the 2D model. k is the intrinsic permeability, ϕ is porosity, D_p is the pore diffusion coefficient and α_L and α_T are the longitudinal and transversal dispersivities.*

	k (m^2)	ϕ_{real}	$\phi_{rescaled}$	D_p (m^2 s^{-1})	α_L (m)	α_T (m)
Fracture	$3.0\cdot10^{-13}$	0.21	0.21	$1.0\cdot10^{-9}$	0.10	0.05
Skin observation	$3.0\cdot10^{-14}$	0.21	0.21	$1.0\cdot10^{-9}$	0.10	0.05
Skin extraction	$3.0\cdot10^{-13}$	0.21	0.21	$1.0\cdot10^{-9}$	0.10	0.05
Gap observation	$3.0\cdot10^{-10}$	1.0	1373.0	$1.0\cdot10^{-9}$	100.0	100.0
Gap extraction	$3.0\cdot10^{-10}$	1.0	612.0	$1.0\cdot10^{-9}$	100.0	100.0

At the outer boundary of the domain a prescribed flux is imposed. The flux is calculated from the flow rates of the three boreholes through the equation

$$\mathbf{q}_b = \frac{1}{2\pi b}\sum_i Q_i \frac{\mathbf{x}_b - \mathbf{x}_i}{\left|\mathbf{x}_b - \mathbf{x}_i\right|^2} \quad i = emp, obs, ext \tag{13}$$

where Q_i (m^3 s^{-1}) is the flow rate at borehole i, b is the fracture thickness (10^{-3} m), $\mathbf{q}_b$ (m^3 m^{-2} s^{-1}) is the Darcy flow vector at the boundary and $\mathbf{x}_b$ and $\mathbf{x}_i$ are the vectors of coordinates of a node at the boundary and of borehole i, respectively. Equation 13 assumes a homogeneous permeability and the flow rates to be located at the center of the boreholes, which is a safe assumption for our model. Flow rates vary in time and are calculated by averaging measured flow rates for periods of 3 months (see Fig. 5). Flow rates for the emplacement and observation boreholes are prescribed using time dependent values, and the values at extraction are calculated by the code (mass balance), matching well the measured data. At the extraction borehole the pressure is fixed at 0.1 MPa (atmospheric pressure).

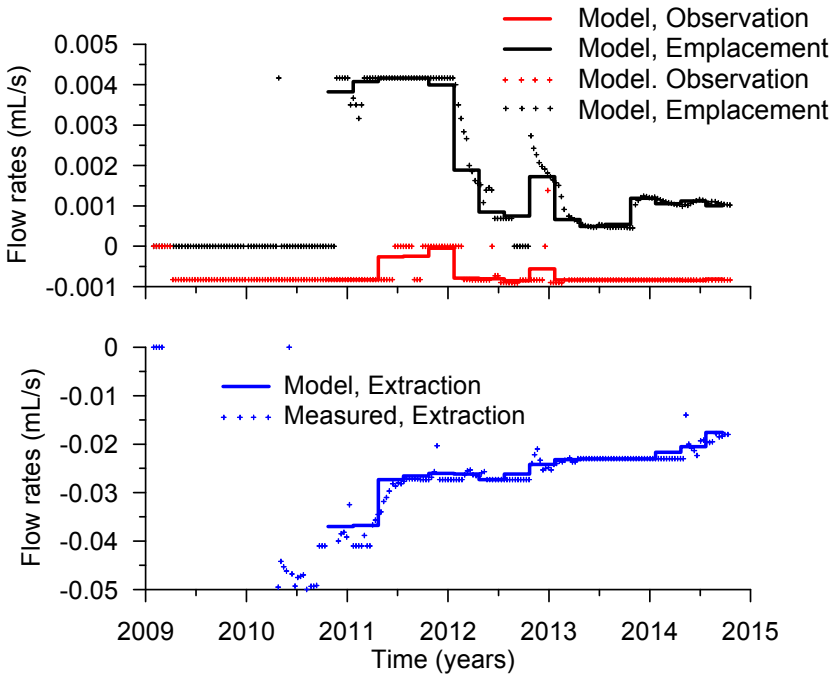

Figure 5. *Measured and modeled flow rates for the three boreholes. Positive values mean injection, negative values extraction.*

4 RESULTS AND DISCUSSION

Before discussing the results of the model, we will first calculate some characteristic times on which transport processes take place. This is helpful for the interpretation of the results of the models. Then we will discuss the results of the 1D radial model that simulates the domain in the vicinity of the emplacement borehole, followed by the results of the 2D model that simulates the domain with three boreholes: emplacement, observation and extraction.

4.1 Characteristic times

A characteristic time for diffusion, t_{dif}, can be defined as

$$t_{dif} = \frac{(L_2 - L_1)^2}{2D_p} \tag{14}$$

where D_p is the pore diffusion coefficient and L_1 and L_2 are the two boundaries between which diffusion takes place. This means that when there are no changes at the boundaries, a steady state is reached after a time of roughly t_{dif}. Equation 14 only makes sense when diffusion is the dominant process, that is, only in the cement and in the skin of the emplacement borehole, the last only during the diffusion period.

A characteristic time for advection, t_{adv}, can be defined in a radial system as

$$t_{adv} = \frac{\pi \phi b \left(L_2^2 - L_1^2\right)}{Q} \tag{15}$$

where ϕ, b and Q are porosity, thickness of the system and injection flow rate, respectively. This means t_{adv} is the time it takes water and a dissolved solute to flow from L_1 to L_2.

A third characteristic time is the average transient time of a solute in an ideally mixed system, t_{mix}.

$$t_{mix} = \frac{V}{Q} \tag{16}$$

where V is the volume of the ideally mixed system. The model volume includes the gap between the dummy cylinder or cement and the borehole wall plus the volume of water circulating in tubes and reservoir tank.

Table 9 shows the calculated characteristic times for the various processes. It can be seen that diffusion in the cement is the slowest process and, therefore, may be the one that controls the system the most. Advection times are short, indicating that water probably will not change its chemistry very much due to precipitation/dissolution of minerals during its passage through the fracture and skins as there is not much time for reactions to occur.

***Table 9**. Characteristic times for the different processes. Characteristic times for diffusion, advection and ideal mixing are calculated by equations 14, 15 and 16, respectively. Characteristic times with two values are calculated from minimum and maximum flow rates.*

Process	Location	Characteristic time (days)
Diffusion (t_{dif})	Cement	383
	Skin of emplacement borehole	7.9
Advection (t_{adv})	Skin of emplacement borehole	0.009 - 0.035
	From emplacement to extraction borehole	0.27 - 0.57
Ideal mixing (t_{mix})	Gap of emplacement borehole	3.4 - 13.7
	Gap of observation borehole	14.6
	Gap of extraction borehole	0.10 - 0.21

4.2 One-dimensional radial model

Figure 6 shows the modeled and measured aqueous chemistry versus time. The behavior during the period of only diffusion (before October 2010) is quite different from the period when water is injected in the gap. During this diffusion period the chemical composition at the skin-fracture interface shows only small changes. That is because the flux of water in the fracture maintains the chemical composition close to that of the natural Grimsel water and the diffusion of cement water is not fast enough to cause an important effect. During the diffusion period the concentrations at the gap rise or fall due to diffusion from or to the cement, respectively. As the characteristic diffusion time in the cement (383 days) is more or less the same as the diffusion period (430 days), changes in concentrations in the gap can still be observed. During injection the concentrations in the gap are practically identical to those at the skin-fracture interface (with the possible exception of Al). The water injected in the gap interacts with the cement and changes only slightly during its passage through the skin, which only takes between 0.009 and 0.035 days (13 and 51 minutes, Table 3). This does not necessarily mean that there is no dissolution or precipitation of minerals, as we will see later. When the injection rate changes to a lower value (June 2011) diffusion from the cement with high pH and Ca concentration has a higher effect as there is less dilution by the injected natural Grimsel water. This results in a higher pH and Ca concentration in both the gap and the skin-fracture interface.

There are some differences between model results and measurements. There can be various reasons for this discrepancy:

- The chemical composition of the Grimsel and cement water as assumed in section 3.2 may be different from reality. This is clearly the case for Cl in Grimsel groundwater (measured and model concentrations are $1.5 \cdot 10^{-4}$ and $4.6 \cdot 10^{-4}$ mol/L, respectively).
- The volume of water in the gap may be larger than originally thought (up to about 1.7 L from the original 1.16 L).
- The pore diffusion coefficient of the cement is based on a guess from previous information. A proper calibration of the diffusion coefficient can improve the match between measurements and the model, since diffusion from the cement is the controlling step of the overall process.

- Cement and cement porewater composition was also assumed from values for a generic cement (Lothenbach and Winnefeld, 2006). These compositions may not be completely accurate.
- The actual injection flow rates show larger variations than the model flow rates. This can also cause higher variation in the model.
- The assumption that no water flow takes place in the skin during the diffusion period may not be entirely true.

Although the match between measurements and model can be improved by changing the model with respect to the above mentioned items, the concept and dominant processes will probably not fundamentally change.

Figures 7 and 8 display the precipitated volume fractions of minerals. Portlandite in the cement dissolves at a sharp dissolution front near the gap (Fig. 7). Note that this front has advanced about only 1 mm in five years. Also C-S-H dissolves and does so at an even smaller rate. During the diffusion period C-S-H, ettringite and some monocarboaluminate precipitate in the skin. C-S-H precipitates near the gap with the same composition as originally found in the cement (Ca/Si = 1.67). After injecting Grimsel water at the gap, these minerals in the skin completely redissolve. Similarly, tobermorite and prehnite precipitate in the skin during the diffusion period (Fig. 8). When Grimsel water is injected they first dissolve, but then precipitate again. Subtle changes in the chemical composition may sometime under- and sometimes over-saturate the water in the skin with respect to these two minerals. Calcite precipitates in the skin near the gap and in the gap itself due to the mixing of Ca and alkalinity from dissolved portlandite and CO_3 from the injected Grimsel water. One can also observe calcite precipitation at the skin-fracture interface. This is the results of the mixing of the injected water reacted with the cement (hence containing much Ca and alkalinity) and Grimsel water (hence containing much CO_3). In our model these two waters mix completely right at the skin-fracture interface. In reality this mixing and ensuing calcite precipitation is probably distributed over a larger area; this large amount of calcite precipitation can be considered a boundary effect. A similar mechanism may be observed for phlogopite due to the mixing of Mg from the Grimsel water and OH^- from dissolution of portlandite in the cement. The primary minerals of the skin except phlogopite (K-feldspar, albite, muscovite and quartz) dissolve due to the high-pH cement conditions.

Figure 9 shows the porosity change due to precipitation and dissolution of minerals. The porosity change in the cement is mainly due to portlandite dissolution and amounts to 0.12, which is the initial volume fraction of the portlandite in the cement. In the skin there is a temporary porosity reduction of about 0.02 due to ettringite precipitation during the diffusion period. During injection the porosity in the skin increases slightly at the end of the simulation due to dissolution of silicate minerals. Porosity decreases right at the gap-rock interface, due mainly to the precipitation of phlogopite.

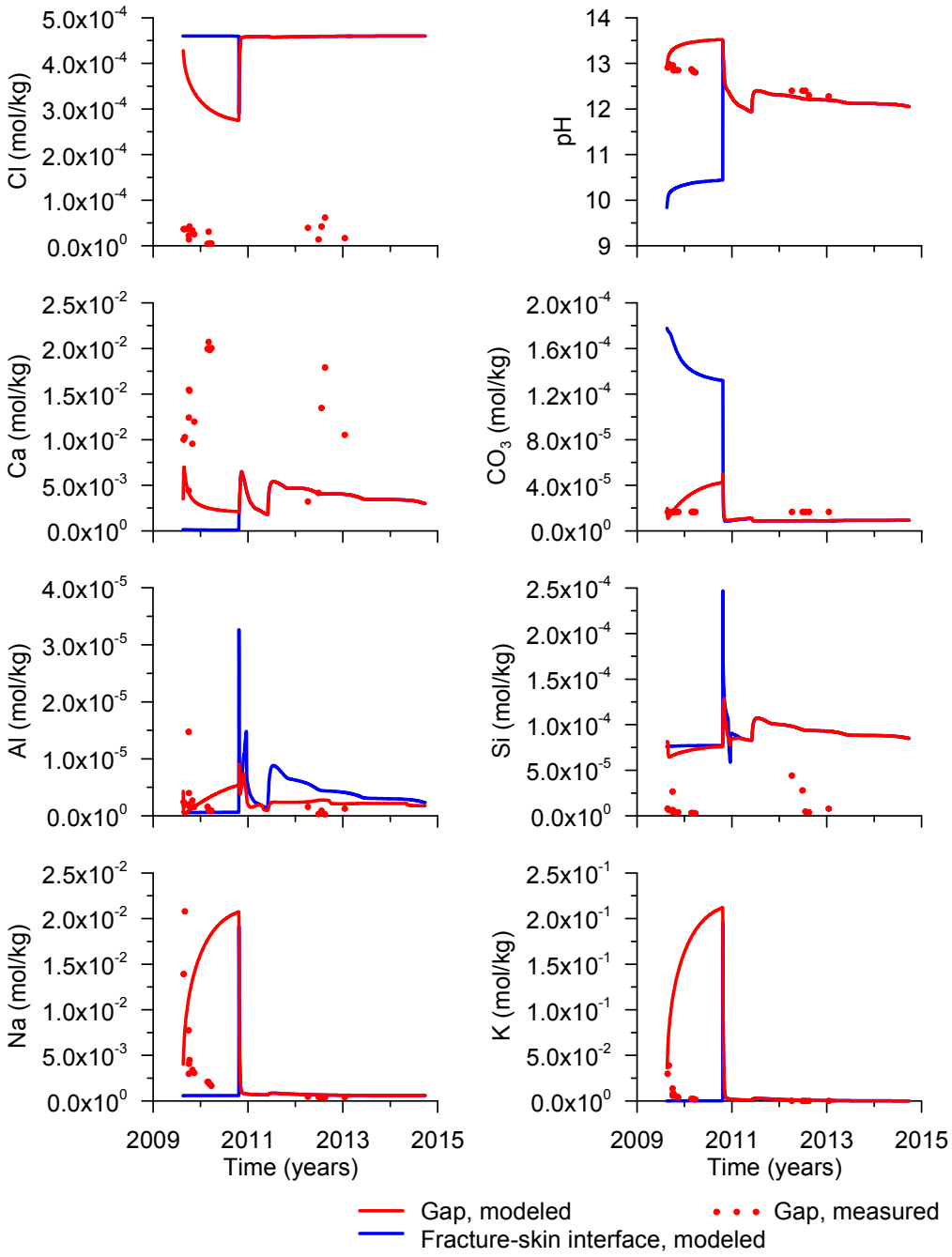

Figure 6. *Modeled and measured total aqueous concentrations and pH versus time for the 1D radial model.*

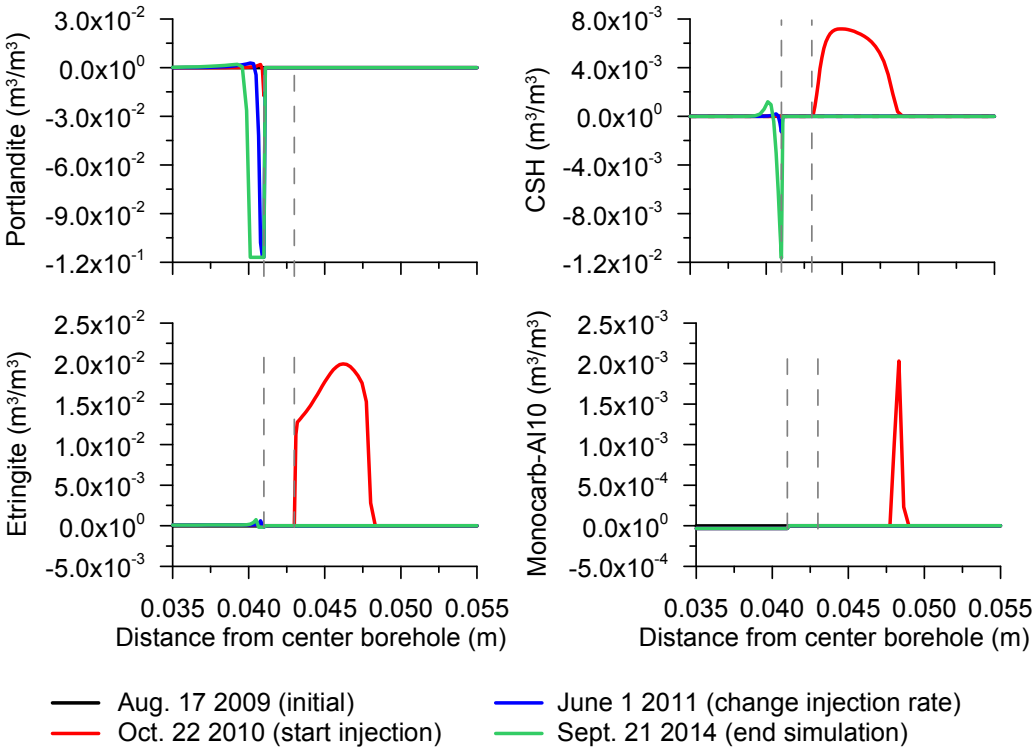

Figure 7. *Modeled precipitated/dissolved volume fractions of portlandite, C-S-H, ettringite and monocarboaluminate (volume of mineral per volume of medium) for the 1D radial model. Positive values indicate precipitation; negative values dissolution. Dashed lines indicate the location of the gap.*

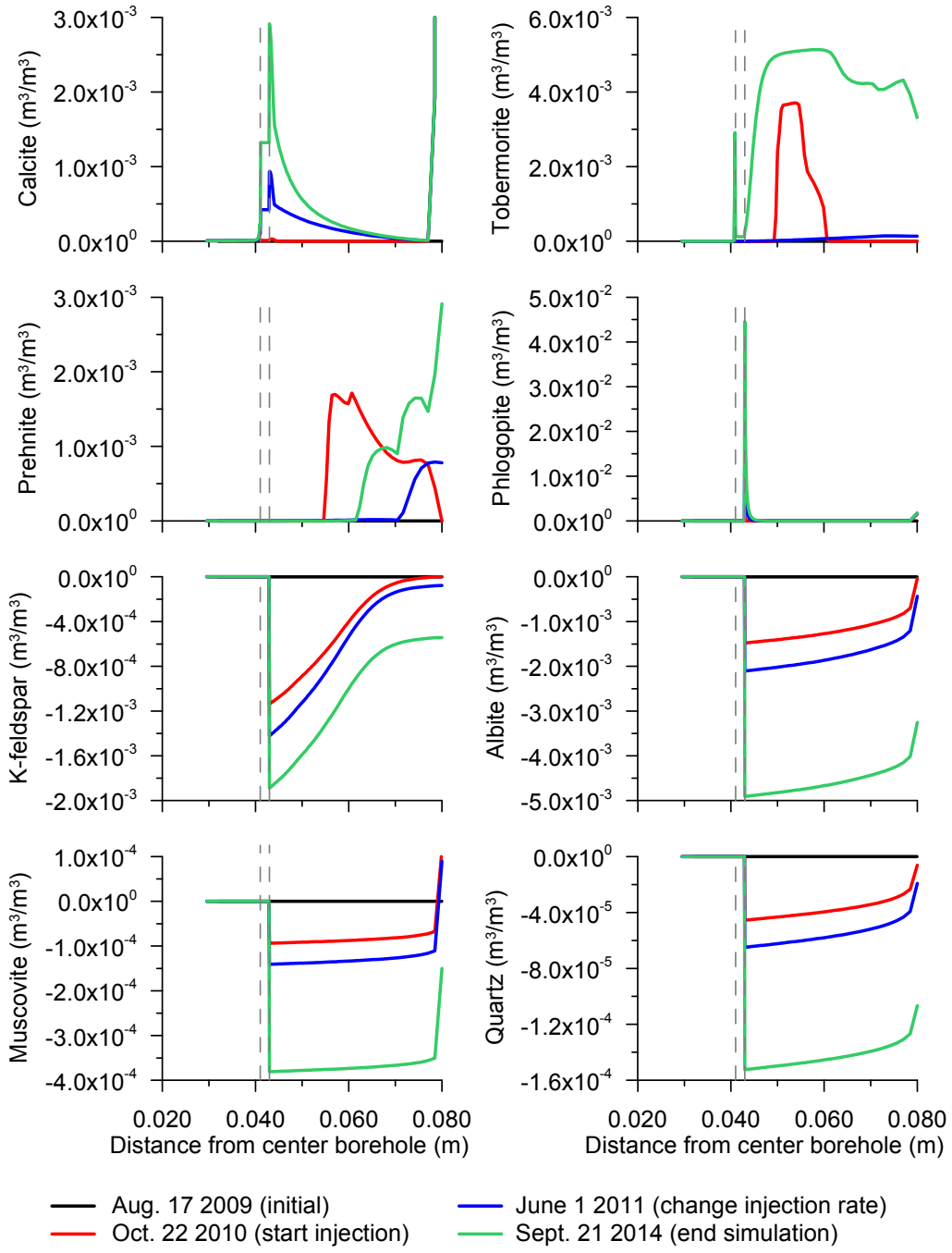

Figure 8. *Modeled change in volume fractions of calcite, tobermorite, prehnite, phlogopite, K-feldspar, albite, muscovite and quartz (volume of mineral per volume of medium) versus distance for the 1D radial model. Positive values indicate precipitation; negative values dissolution. Dashed lines indicate the location of the gap.*

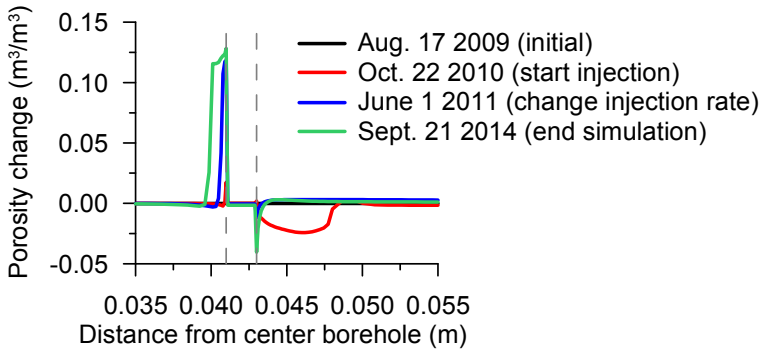

Figure 9. *Porosity change versus distance for the 1D radial model. Dashed lines indicate the location of the gap.*

Figure 10 displays the modeled aqueous chemistry versus space. At the end of the diffusion period (or start of the injection) the gradients of concentrations indicate a diffusion of Cl towards the cement caused by the initially low concentration in the cement. In contrast Na, K and OH^- (pH) diffuse out of the cement. The Ca concentration in the cement shows a peak at the gap, which indicates the dissolution of a mineral containing Ca (portlandite), whereas the CO_3 concentration indicates the precipitation of a mineral containing CO_3 (calcite). Also we can observe the concentrations of Al and Si indicating dissolution of silicates (K-feldspar, albite, muscovite and quartz). The dissolution of K-feldspar, albite and muscovite also affects the concentrations of Na and K, but its effect is less visible because the overall concentrations of Na and K are much higher than those of Al and Si.

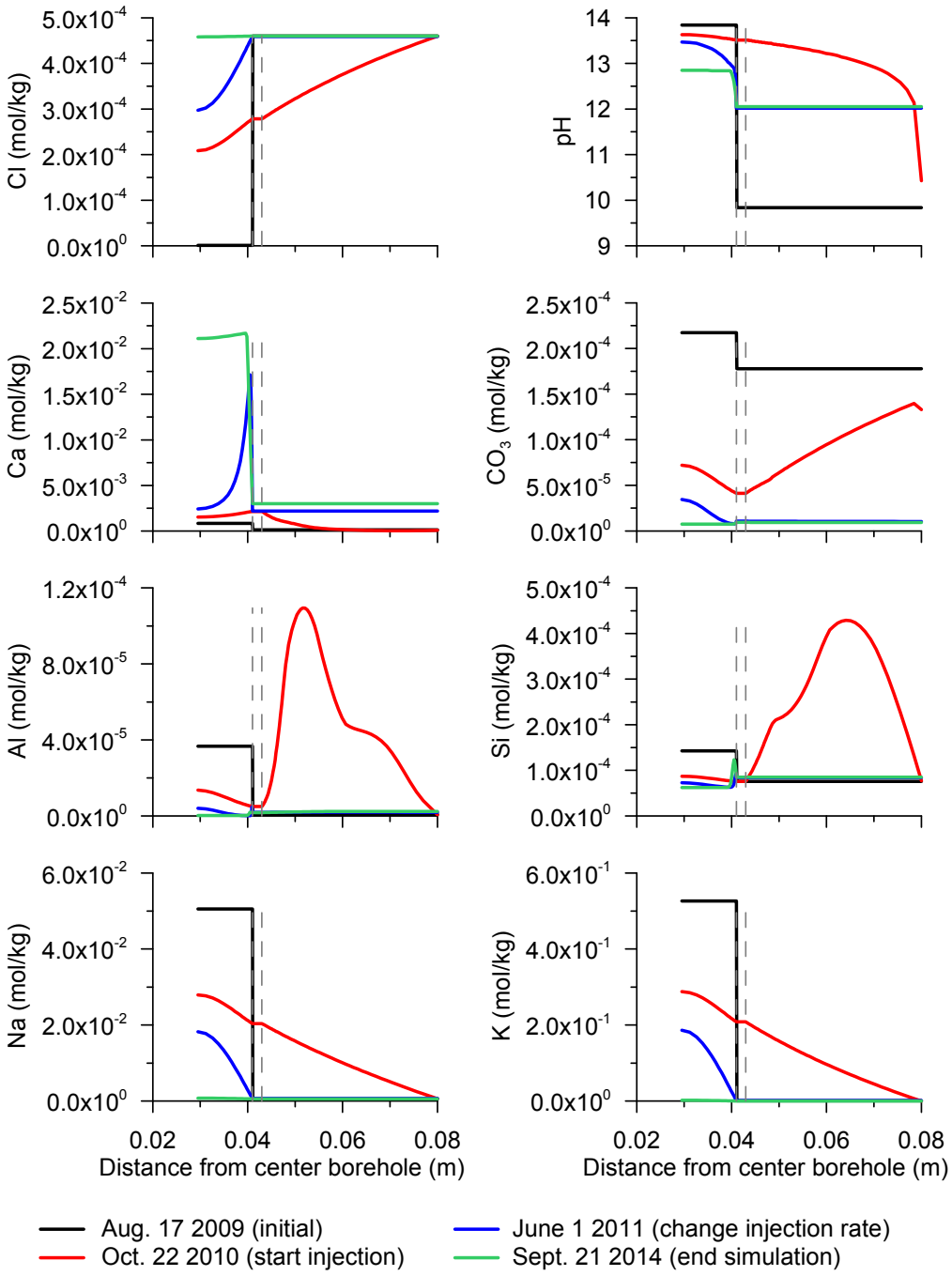

Figure 10. *Modeled total aqueous concentrations and pH versus distance for the 1D radial model. Dashed lines indicate the location of the gap.*

4.3 Two-dimensional model

Table 10 shows the chemical composition of the water at the emplacement borehole skin boundary. This is the water that enters the 2D domain near the emplacement borehole (cement porewater already reacted with rock in the 1D model). From the results of the 1D model, 2 different water compositions have been used at different times ((1) t = 0 to t = 10 d; (2) t > 10 d).

Table 10. *Composition of the water at the emplacement borehole skin boundary for the 2D model.*

	$0 < t \leq 10$ d		$t > 10$ d	
	C_{tot} (molal)	Constraint	C_{tot} (molal)	Constraint
Al	$1.30 \cdot 10^{-5}$		$5.00 \cdot 10^{-6}$	
CO_3	$4.00 \cdot 10^{-5}$		$9.00 \cdot 10^{-6}$	
Ca	$3.00 \cdot 10^{-3}$		$4.00 \cdot 10^{-3}$	
Cl	$3.80 \cdot 10^{-4}$		$1.14 \cdot 10^{-3}$	charge
K	$4.50 \cdot 10^{-2}$	charge	$1.20 \cdot 10^{-3}$	
Mg	$3.40 \cdot 10^{-10}$	phlogopite	$1.66 \cdot 10^{-9}$	phlogopite
Na	$1.00 \cdot 10^{-2}$		$7.00 \cdot 10^{-4}$	
SO_4	$3.00 \cdot 10^{-4}$		$6.00 \cdot 10^{-5}$	
SiO_2(aq)	$1.70 \cdot 10^{-4}$		$9.00 \cdot 10^{-5}$	
pH	13.00		12.20	

Before discussing reactive transport we will first look at flow of water and conservative transport. Figure 11 displays the head distribution. It reveals a pattern of more or less circular isohypses around the extraction borehole and, hence, radial flow, due to the relatively high extraction rates at this borehole. However, the injection of water in the emplacement borehole slightly disturbs the pattern in the vicinity of this borehole. In any case, the pattern shows that all water injected at the emplacement borehole will end up at either the observation or extraction boreholes.

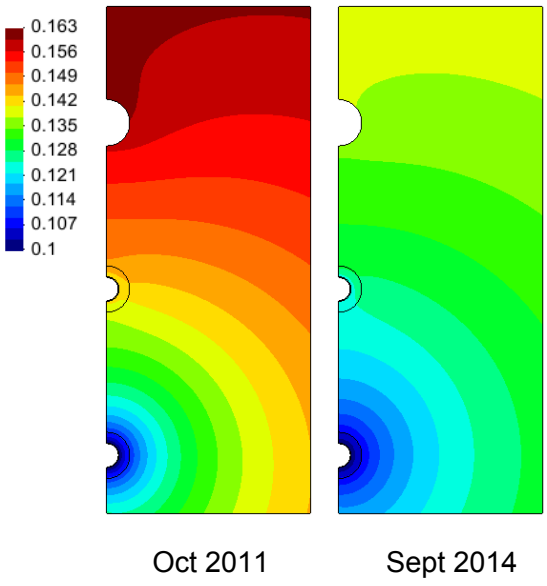

Figure 11. *Head distribution (MPa) at two instants for the 2D model.*

Conservative transport can be characterized by a mixing ratio, λ, between the natural Grimsel water and water reacted with the cement that has been injected at the emplacement borehole. Its value can be calculated from the concentrations of a conservative tracer using

$$\lambda = \frac{c - c_{gri}}{c_{emp} - c_{gri}} \tag{17}$$

where subscripts *emp* and *gri* mean emplacement and Grimsel, respectively. A λ of 0 means pure Grimsel water and a λ of 1 means pure emplacement water reacted with cement. It is worth noting that because all injected water ends up at either the observation or extraction boreholes, at steady state the following must hold:

$$Q_{emp} = Q_{ext}\lambda_{ext} + Q_{obs}\lambda_{obs} \tag{18}$$

where Q means flow rate (magnitude) and subscripts *ext* and *obs* refer to extraction and observation borehole. As Q_{ext} is about 20 to 40 times larger than Q_{obs}, equation 18 can be simplified to $Q_{emp} \approx Q_{ext}\lambda_{ext}$ or

$$\lambda_{ext} \approx Q_{emp} / Q_{ext} \tag{19}$$

Figure 12 displays the mixing ratio versus time. Besides the standard model with dispersivities from Table 8 (α_L = 0.10 m; α_L = 0.05 m), we also studied the effect of lower dispersion (α_L = 0.05 m; α_L = 0.02 m). Obviously, the mixing ratio in the observation borehole is much larger than the extraction borehole, the second being the furthest away from the emplacement borehole. The ups and downs in Fig. 12 are caused by the change in the flow rates of the three boreholes. The mixing ratio in the extraction borehole is basically controlled by flow rates through equation 19 with parameters such as dispersivity having hardly any effect. The mixing ratio in the observation borehole is affected by both dispersivity and flow rates. Figure 12 also shows that it takes a bit more time for the observation borehole to reach a steady state after a change in flow rate than for the extraction borehole due to the larger characteristic time for mixing (Table 9). The distribution of the mixing ratio (Fig. 13) shows that with higher injection rates at the emplacement borehole (October 2011) the size of the plume is larger than for lower injection rates (September 2014). It also shows that the plume is smoother (lines of equal mixing ratio are further away from each other) for higher dispersivities.

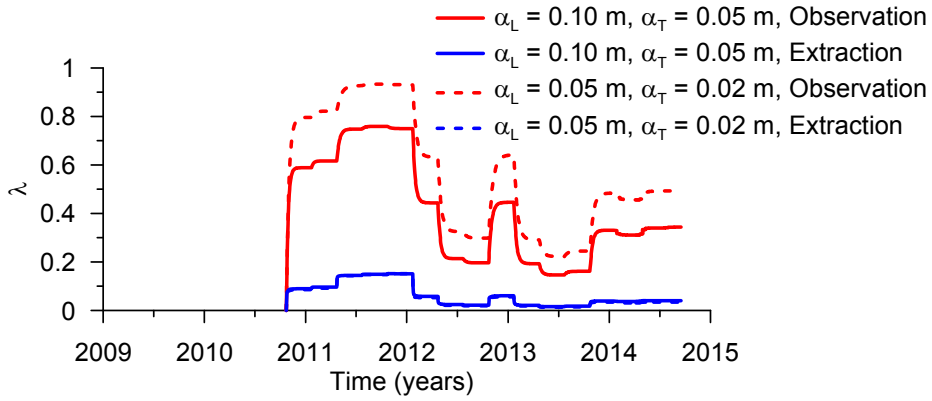

Figure 12. *Mixing ratio (λ) at the two boreholes for the 2D model with different dispersivities.*

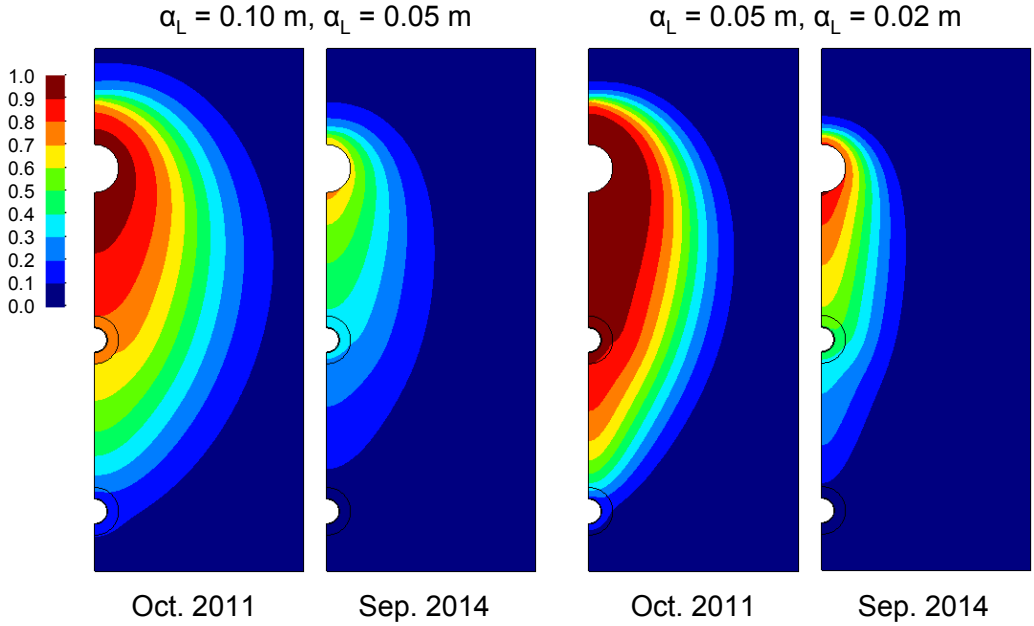

Figure 13. *Mixing ratio distribution at two instants for the 2D model with different dispersivities.*

Figure 14 shows the modeled and measured aqueous chemistry versus time. There is some discrepancy between modeled and measured data. Probably we can attribute it to the same reasons as mentioned for the 1D radial model. Anyway, one can observe that the modeled chemistry oscillates a lot because of the changing flow rates. The same oscillations can be observed for the measured chemistry. So one may conclude that the measured oscillations are not caused by analytical errors or some random outside effect but by changes in the flow rates.

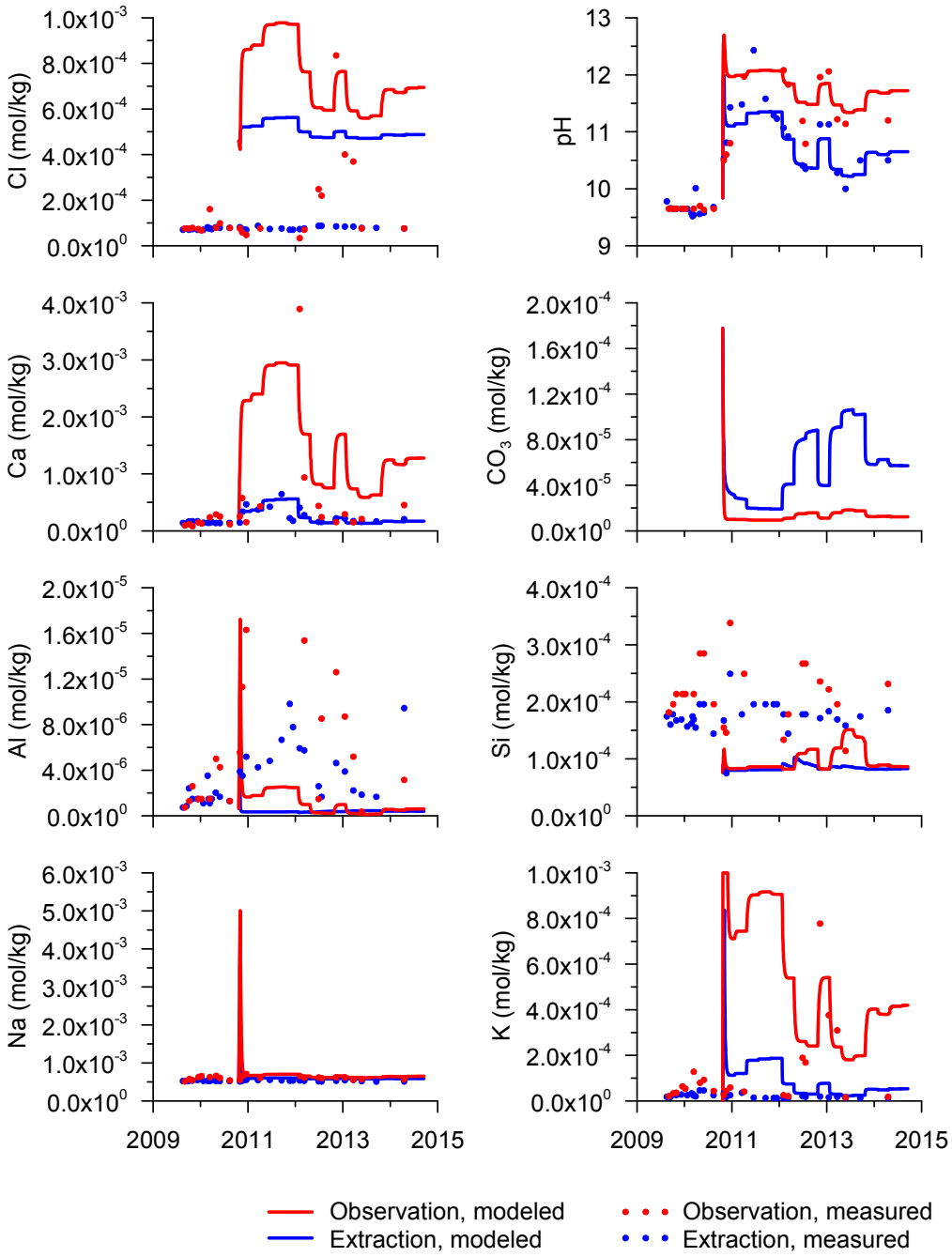

Figure 14. *Modeled and measured total aqueous concentrations and pH versus time for the 2D model.*

Figure 15 displays the precipitated/dissolved volume fractions of minerals. The primary silicate minerals in the fracture (albite, K-feldspar, muscovite, quartz) dissolve due to the increase of pH in the center of the plume. Prehnite and tobermorite precipitate also in the center of the plume. Phlogopite and especially calcite precipitate at the outer edge of the plume. It must be noted that at the end of the simulation calcite almost clogs the fracture near the extraction borehole (Fig. 16) with precipitated volume fractions of up to 0.2.

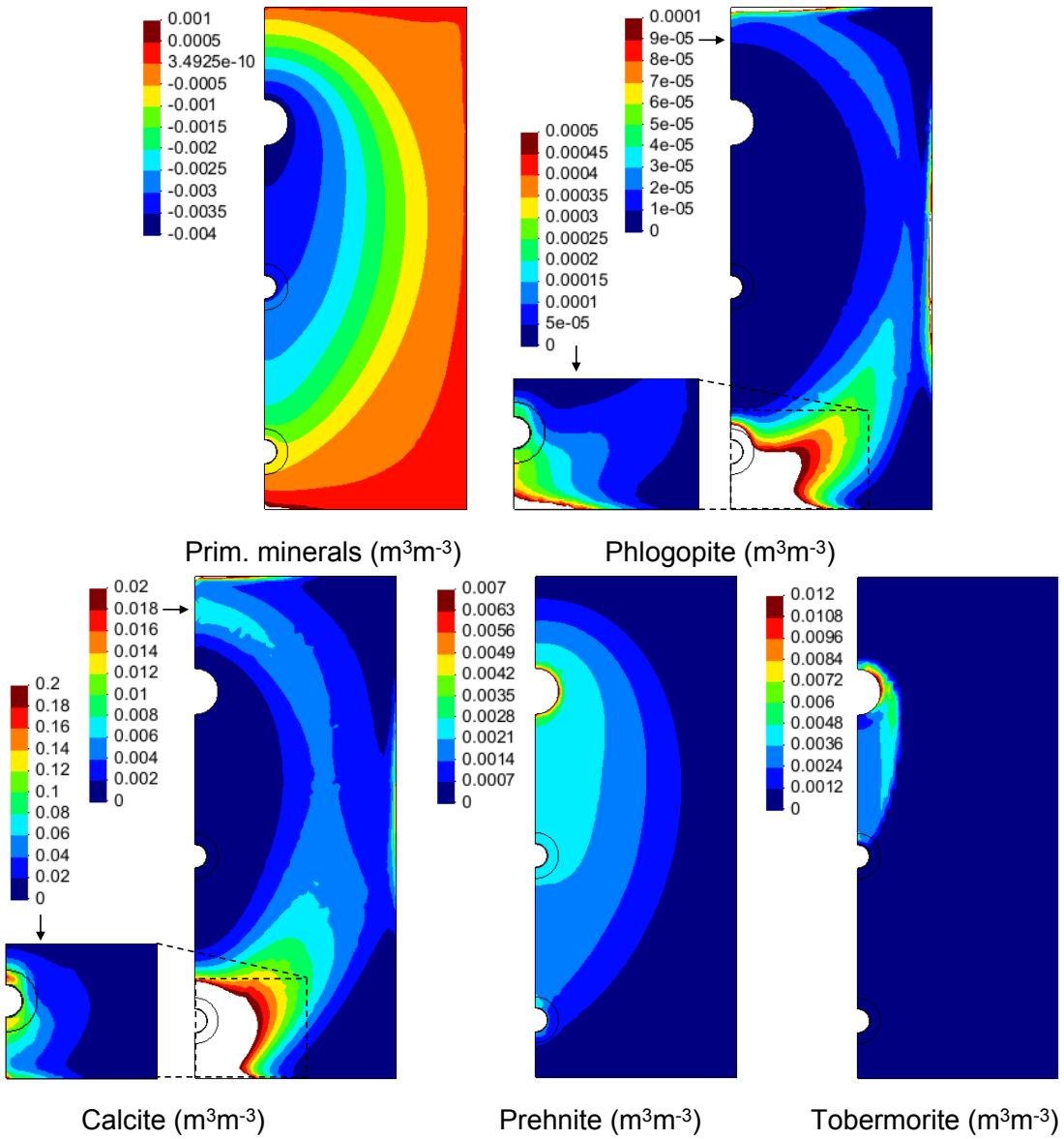

Figure 15. *Distribution of change in mineral volume fraction (volume of mineral per volume of fracture) at the end of the simulation (September 2014). Primary minerals are the sum of albite, K-feldspar, muscovite and quartz. Positive values indicate precipitation; negative values dissolution. For phlogopite and calcite the volume fraction change is particularly high near the extraction borehole. Therefore, that part of the domain is redrawn with another volume fraction scale.*

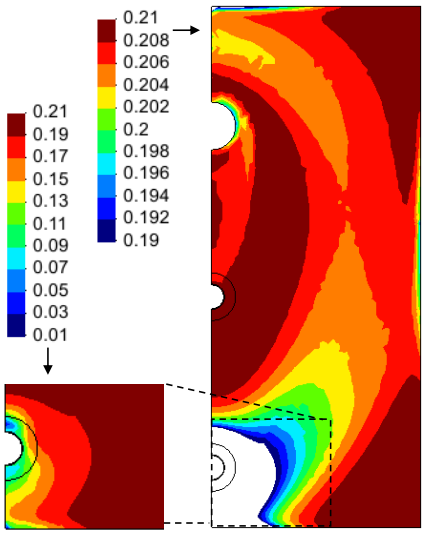

Figure 16. *Model porosities at the end of the simulation (September 2014). Initial porosity is 0.21. The porosity is particularly low near the extraction borehole. Therefore, that part of the domain is redrawn with another porosity scale.*

An interesting question is why calcite precipitates and consequently porosity reduces at the edge of the plume and particularly near the extraction borehole. To analyze this we simplify the chemical system to only one chemical reaction: calcite precipitation-dissolution at equilibrium ($CaCO_3 = Ca^{2+} + CO_3^{2-}$). When two waters are mixed with a different chemical composition but both in equilibrium with calcite, the mixed water tends to be oversaturated with respect to calcite. As a result calcite precipitates reducing Ca and CO_3 concentrations in equal amounts (because of the stoichiometry of the reaction) until equilibrium is reached. We can calculate the new concentrations from the mixing ratio (λ) and the chemical composition of the two end members (emplacement and Grimsel water):

$$\begin{cases} u = c_{Ca} - c_{CO3} = \lambda\left(c_{Ca,emp} - c_{CO3,emp}\right) + \left(1-\lambda\right)\left(c_{Ca,gri} - c_{CO3,gri}\right) \\ c_{Ca}c_{CO3} = K_{cc} \end{cases}$$
$$\Rightarrow \begin{cases} c_{Ca} = \dfrac{1}{2}\left(u + \sqrt{u^2 + 4K_{cc}}\right) \\ c_{CO3} = \dfrac{1}{2}\left(-u + \sqrt{u^2 + 4K_{cc}}\right) \end{cases} \tag{20}$$

where K_{cc} is the equilibrium constant for calcite dissolution-precipitation. According to De Simoni et al. (2005), in the case of transport by advection and dispersion one can calculate the calcite precipitation rate, r, from

$$r = \phi \frac{\partial^2 c_{Ca}}{\partial \lambda^2} \nabla\lambda^T \mathbf{D} \nabla\lambda \tag{21}$$

where $\mathbf{D}$ is the dispersion-diffusion tensor explained in section 2 and c_{Ca} is the Ca concentration. The rate depends on two factors: a chemical factor ($\partial^2 c_{Ca}/\partial\lambda^2$) that can be calculated from equation 20 and a transport factor ($\phi\nabla\lambda^T\mathbf{D}\nabla\lambda$) that can be calculated from the results of conservative transport. Figure 17 shows the calculations of calcite

precipitation rate at the y-axis (axis crossing the three boreholes). The end-member concentrations are taken from section 3.2.2 (Grimsel) and 4.3 (emplacement), shown in Fig. 17a together with the calcite equilibrium ($c_{Ca}c_{CO3} = K_{cc}$). From this, one can calculate the chemical factor ($\partial^2 c_{Ca}/\partial\lambda^2$) as a function of mixing ratio (Fig. 17b). Our particular end-member concentrations give a high chemical factor for a low mixing ratio (i.e., much Grimsel water). Mixing ratios (Fig. 17c) are taken from the numerical model with α_L = 0.10 m and α_L = 0.05 m at the end of the simulation (Fig. 13). This gives high values for the transport factor near the emplacement and extraction boreholes (Fig. 17d) due to the high concentration gradients, $\nabla\lambda$ (for the emplacement borehole) or high dispersion-diffusion coefficients, **D**, due to high velocity of water (for the extraction borehole). The chemical factor is lower at the center of the plume near the emplacement borehole where the mixing ratio is high (Fig. 17e). Multiplication of both factors gives a high value near the extraction borehole, because there both the chemical and transport factors are high (Fig. 17f).

Of course, the chemical system is in reality much more complicated then just one reaction and other reactions have an impact too. Nevertheless, equation 21 and Fig. 17 can give a qualitative explanation of why we found such a high calcite precipitation near the extraction borehole.

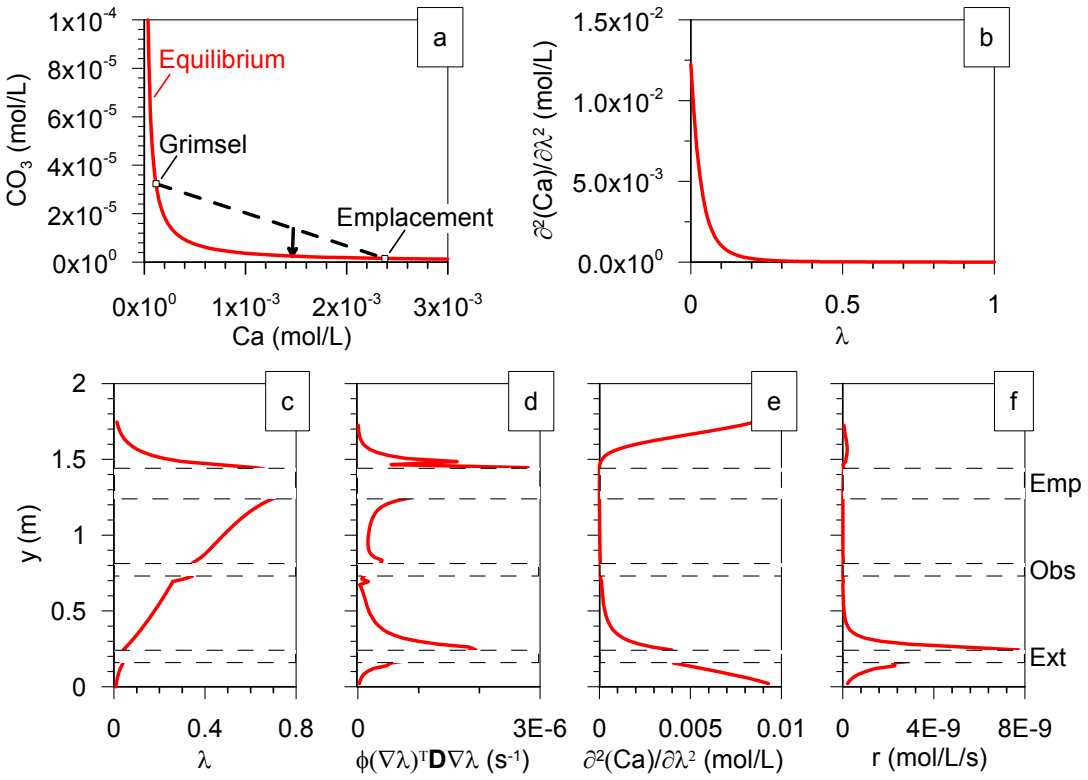

Figure 17. *Calculation of calcite precipitation rate at the y-axis (axis crossing the three boreholes) assuming equilibrium calcite precipitation is the only reaction. Emp, obs and ext refer to emplacement, observation and extraction boreholes.*

5 CONCLUSIONS

Reactive transport modeling of experiment 2 at Grimsel (pre-hardened cement at the emplacement borehole) has been performed using the Retraso-CodeBright software package. Due to the numerical complexity of the problem, modeling has been performed in 2 steps: (1) A 1D radial model simulating the emplacement borehole with the cement and a volume of rock fracture around it (skin, up to a radius of 8 cm). (2) A 2D model starting at the emplacement borehole skin and including the two other boreholes (observation and extraction). The solution composition at the outer boundary of the 1D model has been incorporated into the 2D model as a boundary condition. The changing flow conditions and the different volumes of water in the different boreholes have been taken into account.

Results from the 1D model predict the dissolution of portlandite in a thin (1 mm) outer layer of the cement, with a corresponding increase in porosity. Porosity at the gap-fracture interface is reduced due mainly to the precipitation of phlogopite.

The results from the 2D model show dissolution of the primary silicates (except phlogopite) and precipitation of C-S-H, C-A-S-H and calcite in the fracture. Porosity is reduced in a belt around the 3 boreholes, converging at the extraction borehole (due to the magnitude of the extraction flow rate). The decrease in porosity, due mainly to the precipitation of calcite, is stronger right next to the extraction borehole, due to the more favorable mixing conditions between Grimsel groundwater and cement porewater. The changing water injection rate conditions in the emplacement borehole lead to changes in the flow field and in the position of the mineral reaction fronts.

There are some differences between model results and measurements (water composition at the different boreholes). Factors that can influence these discrepancies are:

- The chemical composition of the Grimsel and cement water used in the model may be different from reality. This is clearly the case for Cl in Grimsel groundwater (measured and model concentrations are $1.5 \cdot 10^{-4}$ and $4.6 \cdot 10^{-4}$ mol/L, respectively).
- The volume of water in the gap at the emplacement borehole may be larger than originally thought (up to about 1.7 L from the original 1.16 L).
- The pore diffusion coefficient of the cement is based on a guess from previous information. A proper calibration of the diffusion coefficient can improve the match between measurements and the model, since diffusion from the cement is the controlling step of the overall process.
- Cement and cement porewater composition was also assumed from values for a generic cement (Lothenbach and Winnefeld, 2006). These compositions may not be completely accurate.
- The actual injection and extraction flow rates at the different boreholes show larger variations than the model flow rates. This can also cause higher variation in the model results.
- The assumption that no water flow takes place in the emplacement borehole skin during the initial diffusion period (zero injection rate) may not be entirely true.

ACKNOWLEDGEMENTS

Discussions with the LCS team, under the lead of Niels Giroud, are gratefully acknowledged. Marja Vuorio kindly translated the abstract into Finnish.

REFERENCES

De Simoni M., Carrera J., Sánchez-Vila X. and Guadagnini A. (2005) A procedure for the solution of multicomponent reactive transport problems. Water Resources Research 41, W11410.

Eikenberg J., Hoehn E., Fierz T. and Frick U. (1994) Grimsel Test Site: Preparation and Performance of Migration Experiments with Radioisotopes of Sodium, Strontium and Iodine. Paul Scherrer Institut Report 94-11.

Hummel W., Berner U., Curti E., Pearson F. J. and Thoenen T, (2002) Nagra/PSI Chemical Thermodynamic Data Base 01/01. Nagra Technical Report 02-16.

Kulik D. A. and Kersten M. (2001) Aqueous solubility diagrams for cementitious waste stabilization systems: II, end-member stoichiometries of ideal calcium silicate hydrate solid solutions. Journal of the American Ceramic Society 84, 3017-3026.

Lanyon G. W. and Giroud N. (2016). LCS Field Experiment 2 (F16): data summary and interpretation (2008-2014). Nagra Working Report NAB 15-07, in preparation.

Lasaga A. C. (1984) Chemical-kinetics of water–rock interactions. Journal of Geophysical Research 89 (Nb6), 4009–4025.

Lothenbach B., Matschei T., Moschner G. and Glasser F. P. (2008) Thermodynamic modelling of the effect of temperature on the hydration and porosity of Portland cement. Cement and Concrete Research 38, 1-18

Lothenbach B. and Winnefeld F. (2006) Thermodynamic modelling of the hydration of Portland cement. Cement and Concrete Research 36, 209-226.

Mäder U. K., Fierz T., Frieg B., Eikenberg J, Rüthi M., Albinsson Y., Möri A., Ekberg S. and Stille P. (2006) Interaction of hyperalkaline fluid with fractured rock: Field and laboratory experiments of the HPF project (Grimsel Test Site, Switzerland). Journal of Geochemical Exploration 90, 68-94.

Manette M., Saaltink M. W. and Soler J. M. (2015). GTS-LCS, In-situ Experiment 2, Modeling of Tracer Test 09-03. Posiva Working Report 2015-05.

Matschei T., Lothenbach B. and Glasser F. P. (2007) Thermodynamic properties of Portland cement hydrates in the system CaO-Al_2O_3-SiO_2-$CaSO_4$-$CaCO_3$-H_2O. Cement and Concrete Research 37, 1379-1410.

Olivella S., Gens A., Carrera J. and Alonso E. E. (1996) Numerical formulation for a simulator (CODE_BRIGHT) for the coupled analysis of saline media. Engineering Computations 13, 87-112.

Saaltink M. W., Batlle F., Ayora C., Carrera J. and Olivella S. (2004) RETRASO, a code for modeling reactive transport in saturated and unsaturated porous media. Geologica Acta 2, 235-251.

Savage D., Soler J. M., Yamaguchi K., Walker C., Honda A., Inagaki M., Watson C., Wilson J., Benbow S., Gaus I. and Rueedi J. (2011) A comparative study of the modelling of cement hydration and cement–rock laboratory experiments. Applied Geochemistry 26, 1138-1152.

Soler J. M. and Lasaga A. C. (1998) An advection-dispersion-reaction model of bauxite formation. Journal of Hydrology 209, 311-330.

Soler J. M. and Mäder U. K. (2007) Mineralogical alteration and associated permeability changes induced by a high-pH plume: Modeling of a granite core infiltration experiment. Applied Geochemistry 22, 17-29.

Soler J. M. and Mäder U. K. (2010) Cement-rock interaction: Infiltration of a high-pH solution into a fractured granite core. Geologica Acta 8, 221-233.

Soler J. M., Pfingsten W., Paris B., Mäder U. K., Frieg B., Neall F., Källvenius G., Yui M., Yoshida Y., Shi P., Rochelle Ch. A. and Noy D. J. (2006) HPF Experiment: Modelling Report. Nagra Technical Report 05-01.

Trapote-Barreira A., Cama J., Soler J. M. and Lothenbach B. (2016) Degradation of mortar under advective flow: Column experiments and reactive transport modeling. Cement and Concrete Research 81, 81-93.

Walker C. S. (2016) Porosities and Effective Diffusion Coefficients in Hydrated Portland Cement Pastes. Nagra Working Report NAB 16-04.

Wolery T. J., Jackson K. J., Bourcier W. L., Bruton C. J., Viani B. E., Knauss K.G. and Delany J. M. (1990) Current status of the EQ3/6 software package for geochemical modeling. In: Melchior C. & Bassett R. L. (Eds.) Chemical Modeling of Aqueous Systems II. ACS Symposium Series No 416, pp. 104-116.